Available online at www.CivileJournal.org

Civil Engineering Journal

(E-ISSN: 2476-3055; ISSN: 2676-6957)

Vol. 8, No. 10, October, 2022

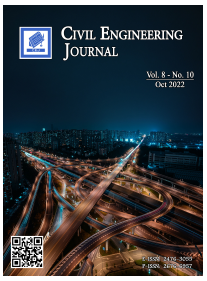

Forecasting the Effects of Failure Criteria in Assessing Ship Structural Damage Modes

Aditya Rio Prabowo [1*], R. Ridwan [2], T. Tuswan [3], Fitrian Imaduddin [1, 4*]

[1] *Department of Mechanical Engineering, Universitas Sebelas Maret, Surakarta 51276, Indonesia.*

[2] *Department of Mechanical Engineering, Universitas Merdeka Madiun, Madiun 63133, Indonesia.*

[3] *Department of Naval Architecture, Universitas Diponegoro, Semarang 50275, Indonesia.*

[4] *Department of Mechanical Engineering, Islamic University of Madinah, Medina 42351, Saudi Arabia.*

Received 16 July 2022; Revised 22 September 2022; Accepted 27 September 2022; Published 01 October 2022

Abstract

The failure to achieve satisfactory results will cause immense losses in major projects. Nevertheless, the modeling limitations and phenomenon assumptions represented by failure criteria can significantly influence the final results—e.g., the damage mode, affecting its quantification—thus representing an interesting topic for technical assessment. This work aims to forecast the effects of several failure criteria on the damage occurring due to structural loading schemes, such as compression, torsion, and tensile tests. Failure criteria are taken based on the proposal of pioneer researchers and include those of Peschmann (P), Germanischer Lloyd (GL), Liu (LIU), and Rice–Tracey and Cockroft–Latham (RTCL). A series of nonlinear finite element analyses (NLFEA) are conducted by inputting these criteria into different loading schemes. To obtain reliable validation, the proposed models are designed based on previous laboratory experiments. The numerical results of NLFEA in the forms of damage mode, i.e., tearing, plastic deformation, and torsion, are cross-checked with experimental data. The results show that numerical modeling using the LIU criterion produces slightly larger discrepancies compared with experimental data. This indication is founded on the analysis of stress–strain, load–displacement, and shear stress–strain during the tensile test, compressive load, and torsion load, respectively. According to this work, we formulate recommendations based on the forecast tendency and accuracy for each damage mode subjected to failure criteria. Therefore, future works can adopt the findings in our current work when choosing to apply specific criteria in structural modeling and load idealization.

Keywords: Failure Criteria; Damage Modes; Loading Schemes; Nonlinear FEA; Engineering Structures; Structural Damage.

1. Introduction

Ships are an essential component in the world and a fundamental part of world trade. In 2020, international maritime trade will reach nearly 10.7 billion tons. However, this value is slightly lower than in 2019, as the COVID-19 pandemic sequentially disrupted supply, demand, and logistics [1]. In 2019, international maritime trade reached 11.2 billion tons. Reviews of safety and shipping review at the end of 2020 show 49 ship losses worldwide, which in the previous year were 48 [2]. This catastrophe is represented by numerous causes such as fire/explosion, collision, grounding, hull damage, and machinery damage/failure resulting in such damage as tearing, plastic deformation, folding, and torsion. Research to improve the safety of transportation [3], especially ships, has been critical in recent years [4-7]. The methods introduced by researchers for analyzing the structural damage in a ship can be classified into four categories: empirical

* Corresponding author: aditya@ft.uns.ac.id; fitrian@ft.uns.ac.id

http://dx.doi.org/10.28991/CEJ-2022-08-10-03

methods [8], finite element methods [9-12], experimental methods, and simplified analytical methods. Numerous researchers have introduced various criteria used in finite element methods, such as Peschmann (P) [9], Germanischer Lloyd (GL) [10], Rice–Tracey and Cockcroft–Latham (RTCL) [11], and Liu (LIU) [12]. However, the use of these criteria to date is still general; for example, criteria they have all been used when only focusing on tearing damage [13].

Several research works have been devoted to assessing failure criteria in ship accidents using nonlinear finite element analysis. Ehlers et al. (2008) [14] studied the collision response of shipside structures employing the Germanischer Lloyd (GL), Peschmann (P), and Rice–Tracey and Cockcroft–Latham (RTCL) criterion, in which the force–penetration curve based on the inner mechanics was determined. In the following year, the study conducted by Alsos et al. (2009) [15] used the Rice–Tracey and Cockcroft–Latham (RTCL) criterion for determining the resistance to penetration of stiffened plates. Hull plates in ships subjected to grounding or collision actions were studied, and the failure mechanisms were quantified and discussed. Similarly, in the numerical study carried out by Marinatos & Samuelides (2015) [16], the Rice–Tracey and Cockcroft–Latham (RTCL) criterion was used to examine the failure mode in collisions and groundings of ships. Both the force and the absorbed energy during these accidents were discussed. Further works regarding failure criteria in ship accidents can also be found in [17-19]. Although most previous investigations have been reviewed in exploring failure criteria, there is limited study concerning the evaluation of several failure criteria to investigate the behavior distinction of numerical modeling under different loading schemes, including through tensile, compressive, and torsional tests. Moreover, the research regarding employing failure criteria on the behavior of these damage mechanisms is still scarce.

In this study, the use of Peschmann (P), Germanischer Lloyd (GL), Liu (LIU), and Rice–Tracey and Cockroft–Latham (RTCL) as failure criteria will be examined using nonlinear finite element (FE) analysis to investigate failure characteristics. The types of damage include tearing, plastic deformation, folding, and torsion. A benchmark study with previous experimental tests will be conducted to check the validity of the evaluated failure criteria.

2. Fundamentals of Mechanical Damage

2.1. Tensile Load

A failure in tensile load refers to failure related to the tensile load occurring at the end of the specimen, Figure 1-a. The specimens used in testing will be deformed according to the ultimate strength and then fail at the end of the test. The middle of the specimen is the original gauge length l_0, and represents the location where failure is expected. During the test, the applied load F and the elongation $\Delta L = l - l_0$ will be recorded. The load F is divided by the original cross-sectional area of specimen A_0 and the elongation ΔL by the original gauge length l_0. The engineering stress $\varepsilon_{eng.}$ is defined as:

$$\sigma_{eng.} = \frac{F}{A_0} \tag{1}$$

The engineering strain $\varepsilon_{eng.}$ is defined as:

$$\varepsilon_{eng.} = \frac{\Delta L}{l_0} \tag{2}$$

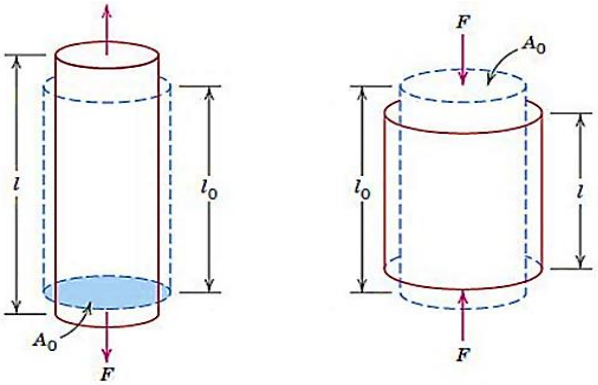

Figure 1. (a) Illustration of tensile load and (b) lustration of compressive load [20]

2.2. Compressive Load

Similar to tensile loads, compressive loads are the loads that are applied to a specimen. The difference occurs in the direction of the working load, whereas in the compressive load, the load works in the negative direction, Figure 1-b. The equations to determine the compressive stress and strain are Equations 1 and 2, respectively. Different conditions are applied a to load F, which is a negative compressive load. Furthermore, the compressive strain is also negative.

2.3. Torsional Load

Torsion load can determine the mechanical properties of a material, such as its torsional shear stress, maximum torque, shear modulus, and angle of break. The specimen used is a cylindrical solid object (axisymmetric). In this test, the specimen is placed on a torque tester, and one end of the specimen is rotated about the long axis until failure occurs, Figure 2. The moment that causes this twisting is the torque. In Figure 2, the torque causes one end of the specimen to rotate, which results in the angle of twist angle, ϕ. It can be calculated using Equation 3. T and L are the applied torque and cylindrical length, respectively. G and J are the shear modulus and polar moment of inertia.

$$\phi = \frac{TL}{GJ} \tag{3}$$

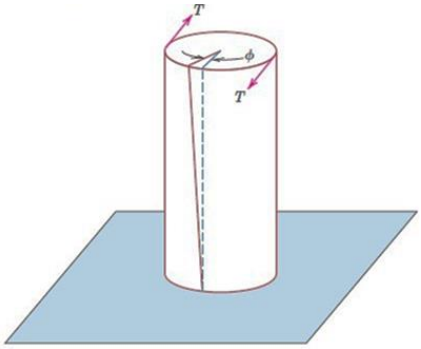

Figure 2. Illustration of torsional load [20]

3. Brief of Finite Element Approach

Nonlinear finite element analysis (NLFEA) is conducted using ANSYS LS-DYNA [21]. The algorithm used corresponds to Equations 4-8, where $\{a_t\}$ is the acceleration; $\{F_t^{ext}\}$ and $\{F_t^{int}\}$ are the applied external and body force vector and the internal force vector, respectively; F^{cont} is the contact force; F^{hg} is the hourglass resistance force; and B^T is the form identical to the linear discrete strain–displacement matrix. σ_n is the internal stress, Ω is the solid volume, $\{v_t\}$ is the velocity at time *t*; $\{u_t\}$ is the displacement at time *t*; $\{x_0\}$ is the initial geometry; $\{x_t\}$ is the updated geometry at time *t*; and Δt_t is the difference in time of at time *t* compared to the initial condition.

$$\{a_t\} = [M]^{-1}\left(\{F_t^{ext}\} - \{F_t^{int}\}\right) \tag{4}$$

$$F^{int} = \sum\left(\int_{\Omega}(B^T\sigma_n d\Omega + F^{hg}) + F^{cont}\right) \tag{5}$$

$$\{v_{t+\Delta t/2}\} = \{v_{t-\Delta t/2}\} + \{a_t\}\Delta t_t \tag{6}$$

$$\{u_{t+\Delta t}\} = \{u_t\} + \{v_{t+\Delta t/2}\}\Delta t_{t+\Delta t/2} \tag{7}$$

$$\{x_{t+\Delta t}\} = \{x_0\} + \{u_{t+\Delta t}\} \tag{8}$$

The simulation is carried out with the following instrument specifications: 4th Generation Intel Core i7-4790 Processor 4.00 GHz with 16 GB of RAM.

4. Failure Criteria Definition

4.1. Germanischer Lloyd (GL)

The Germanischer Lloyd (GL) criterion was proposed by Scharrer et al. (2002) [10]. This criterion is based on the through-thickness strain experiment of the damaged plate which is adapted from the actual structure of the ship that experienced a collision and grounding accident. The Germanischer Lloyd (GL) criterion assumes that the element at the moment of fracture can be expressed in the following form:

$$\varepsilon_f(l_e) = \varepsilon_g + \varepsilon_e\left(\frac{t}{l_e}\right) \tag{9}$$

where ε_g and ε_e are the uniform strain and the necking strain, respectively. t is the thickness of the plate and l_e is the length of the element. The upcoming values of uniforms strain and necking strains are typical for mild steel material utilize in shipbuilding: ε_g = 0.056 and ε_e = 0.54 for plate structure and ε_g = 0.079 and ε_e = 0.76 for beams or trusses.

4.2. Peschmann (PESC)

The Peschmann criterion was proposed by Lehman & Peschmann (2002) [9]. This criterion was derived from experimental results that evaluate the plastic strain of the ship that experienced the accidents. The equivalent plastic strain that is to be applied according to the presented equation:

$$\varepsilon_f(l_e) = \varepsilon_g + \alpha\left(\frac{t}{l_e}\right) \tag{10}$$

here, ε_g and $\alpha = \varepsilon_m \cdot (x_e/t)$ are the uniform strain and a factor that depends on the necking strain and length of the neck, respectively. t is the thickness of the plate and l_e is the length of the element. The $\frac{l_e}{t}$ ratio is usually not less than 5 for shell elements. For plate thickness of ≤ 12 mm: ε_g = 0.1 and α = 0.8. For plate thickness > 12 mm: ε_g = 0.08 and α = 0.65.

4.3. Rice–Tracey and Cockcroft–Latham (RTCL)

The Rice–Tracey and Cockcroft–Latham (RTCL) criterion was first proposed by Törnqvist (2003) [11]. This criterion is based on the combination of two continuum damage models which are the Rice–Tracey [22] and Cockcroft–Latham [23] damage models. The Rice and Tracey criterion is established on void growth and coalescence. On the other hand, the Cockcroft–Latham criterion corresponds to failure by shear under small stress triaxiality. These two-damage models cover the full stress triaxiality range that distinguishes between compression, shear, and tension-dominated damage. The RTCL equation is as follows:

$$\dot{D} = \begin{cases} 0 & T < -1/3 \quad (compression) \\ \frac{\sigma_1}{\sigma_{eq}}\dot{\varepsilon}_{eq} & -1/3 \le T < 1/3 \quad (shear) \\ exp\left(\frac{3T-1}{2}\right)\dot{\varepsilon}_{eq}\ (if\ 1/3 & 1/3 \le T \quad (tension) \end{cases} \tag{11}$$

where $\dot{D}$ is the damage rate, and D can be defined as:

$$D = \frac{1}{\varepsilon_{cr}}\int \dot{D}dt \tag{12}$$

here, ε_{cr} is critical strain in which mesh scaled by the following expression

$$\varepsilon_{cr} = n + (\varepsilon_n - n)\left(\frac{t}{l_e}\right) \tag{13}$$

where n is the power-law exponent and $\varepsilon_n$is the failure strain in terms of uniaxial tension for a mesh size $l_e = t$.

4.4. Liu Formula (LIU)

The Liu criterion was first proposed by Liu et al. (2017) [12], which suggests that the failure strain can be determined using the following equation:

$$\varepsilon_f = 0.5 - 0.01\left(\frac{l}{t}\right) \tag{15}$$

where t and l_e are the plate thickness and the length of the elements, respectively. As shown, LIU criterion gives the necking strain corresponding to 0.50. As suggested, the ratio *l/t* should range between 5 and 20.

5. Benchmarking Particulars

5.1. Benchmark Profiles

The experimental tensile test conducted by Cabezas & Celentano (2004) [24] was re-conducted in this study. The specimens used are shown in Figure 3. The specimens have a length of 200 mm, a grip length of 50 mm, and a grip width of 20 mm each. Moreover, the specimen was prepared with 6 mm thickness. The manufacturing material that was used is SAE 1045 steel. The mechanical properties of SAE 1045 steel are summarized as follows: the ultimate stress σ_u of 762.0 MPa, yield stress σ_y 451.6 MPa, and failure strain ε_f 0.2. The second benchmark was a thin-walled hollow structure subject to a compression loading experiment [25]. Loading was conducted using the SHIMADZU Universal Testing Machine (UTM). Test specimens were thin-walled squares of aluminum tubes with a size of 38 mm x 38 mm and a thickness of 1.2 mm. The mechanical properties of aluminum material had a density ρ of 2700 kg/cm^3, a Young's modulus E of 68 GPa, and a Poisson's ratio υ of 0.33. The overall length of the test specimen was 95 mm. The specimens were compressed with a steel press head until 47.5 mm downward. The loading scheme is shown in Figure 4.

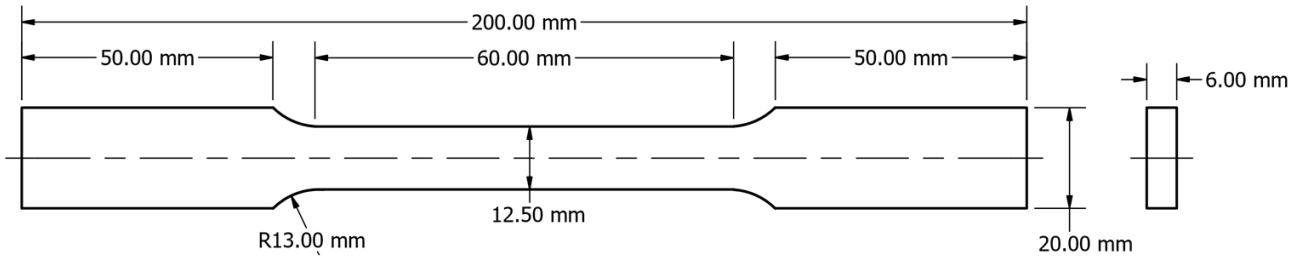

Figure 3. Dimensions of the specimen based on [24]

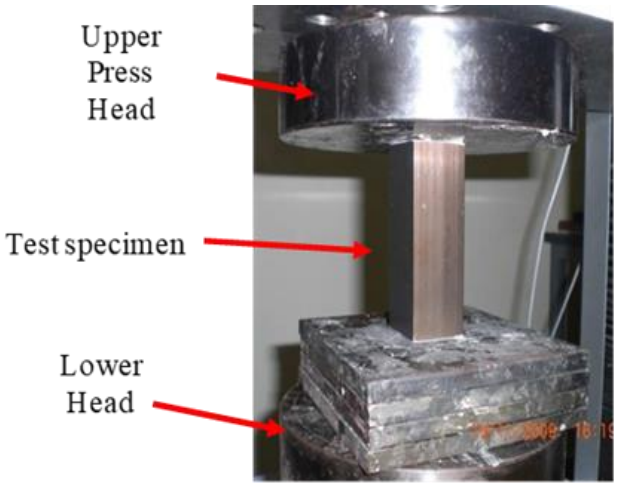

Figure 4. Experimental of the hollow structure under compression loading [25]

5.2. Benchmark Results

The current simulation is performed using nonlinear finite element analysis (NLFEA) ANSYS LS-DYNA [21]. For the tensile test, the specimen (Figure 3) is discretized using 1-10 mm of mesh size with shell-type elements, which are manufactured using SAE 1045 steel material. The boundary condition is applied in two conditions i.e., translation constraint and displacement. The translation constraint is applied at the end of $x-$ coordinate grip section and set to be in the $Ux-$, $Uy-$, and $Uz-$directions equal to fixed. On the other hand, the displacement is applied at the other end grip section and set to be in the $Ux-$ equal to free, $Uy-$, and Uz-directions equal to fixed. The displacement is performed in the opposite direction from the specimen and the simulation ends when the specimen experiences failure. For the simulation of the hollow structure under compression loading, the specimen test (Figure 4) is discretized using 2-10 mm mesh size also with shell-type elements, which are manufactured using aluminum material. The boundary condition is applied in two conditions, i.e., translation constraint and displacement. The translation constraint is applied at the bottom of the specimen, which is set to be in the $Ux-$, $Uy-$, and $Uz-$directions equal to fixed. The displacement is applied on the steel press, which is set to be in the $Uy-$ and $Uz-$directions equal to fixed, and $Ux-$directions equal to free. Moreover, 47.5 mm of displacement is applied downward in the $x-$direction.

Figure 5 shows the comparison of stress–strain curve of the experimental data and simulation of tensile test. The mesh convergence study with 10 variations of the element-length-to-thickness (ELT) ratio is shown in Figure 6. It can be seen from Figures 5 and 6 that 1-5 mm ELT ratios show a relative convergence when compared with the experimental results. These results are quite satisfactory when compared with the experiment data. The highest difference occurred when ELT 10 mm was used, which gives ultimate and yield stresses of 757 and 472 MPa, respectively. Compared to the experimental results, these values have a difference of 5 and 20.4 MPa, respectively, representing percentage errors of around only 0.65% and 4.23%, respectively.

The load–displacement curve of the hollow structure under compression loading is shown in Figure 7. The maximum force shows a value of 29.5 kN for all ELT ratios, a difference of 1.64 kN lower compared with the experimental value of 31.14 kN. This corresponds to a percentage difference of around 5.4%. The 10 mm ELT ratio seems to have a nearly linear trend from 15 to 35 mm displacement. This phenomenon is inversely proportional to the experimental data. It shows that 2 mm mesh has a similar load vs. displacement curve trend compared to the experimental data. It is revealed that mesh size selection is a crucial aspect in terms of numerical modeling verification [26-29].

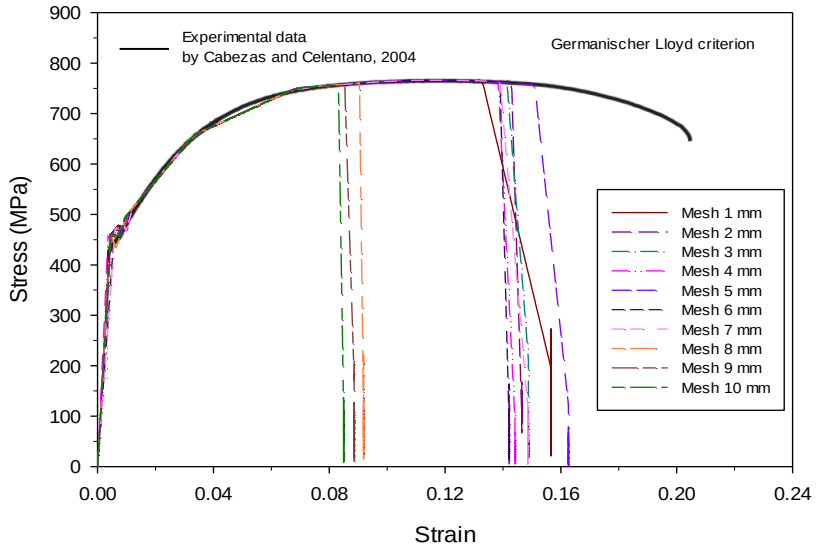

Figure 5. Stress vs. strain curve of the tensile test

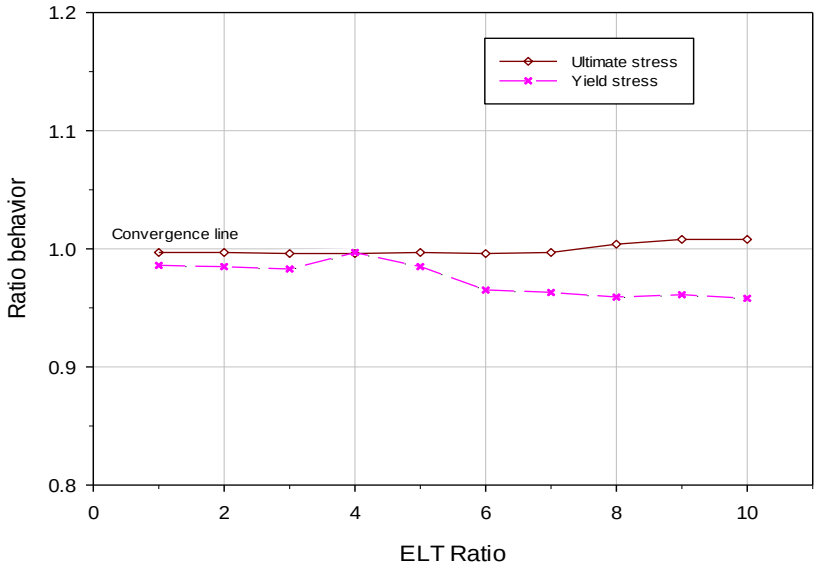

Figure 6. Mesh convergence ratio of ultimate and yield stress

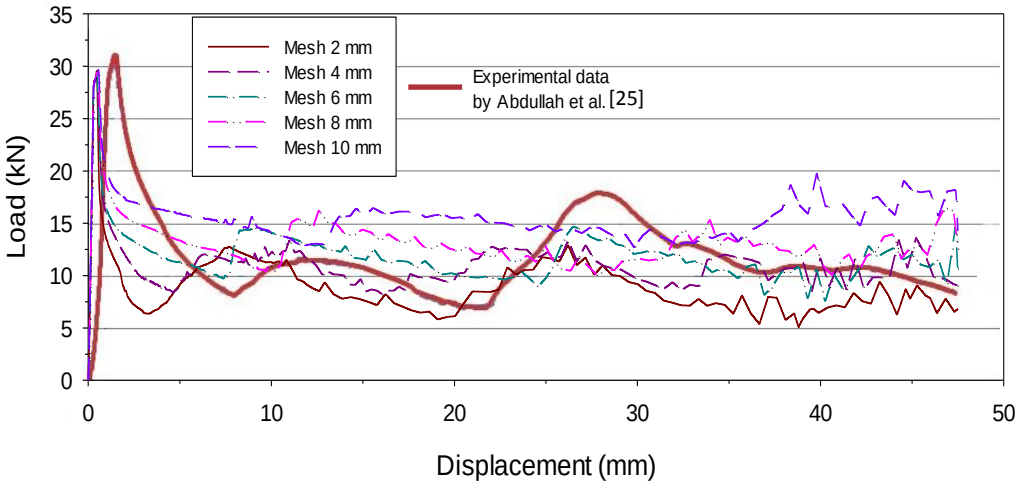

Figure 7. Load vs. displacement curve of the compressive test

6. FE Preparation and Configuration

Finite element analysis is conducted for several numerical tests: tensile, compressive, and torsion tests. The FE pre-processing stage defines geometrical modeling, material input, and load scheme. A comprehensive overview of

specimen geometries and applied load and boundary conditions are determined as shown in Figure 8. The dimensions of the tensile test specimen are similar to previous work [24], with a length of 200 mm, grip width of 20 mm, grip length of 50 mm, and thickness of 6 mm, as shown in Figure 3. The boundary condition is set the same as for the experimental test, where the fixed support is applied in one grip, and displacement load in the opposite direction is applied in the other grip. For the fixed support, the translation constraint is applied in $Ux-$, $Uy-$, and $Uz-$directions equal to fixed. On the other grip, the displacement applied in the $Ux-$direction is equal to free, and in the $Uy-$ and $Uz-$directions equal to fixed, Figure 8-a. The displacement is performed in the opposite direction from the specimen and the simulation ends until the specimen experiences failure. Moreover, the geometrical parameters and numerical setup for the compressive test are similar to the previous experimental test [25]. The test specimen has a size of 38 mm x 38 mm, a length of 98 mm, and a thickness of 1.2 mm, as illustrated in Figure 8-b. The translation constraint is applied at the bottom of the specimen, which is set in the $Ux-$, $Uy-$, and $Uz-$directions equal to fixed. The displacement is applied on the steel plate, which is set in the $Uy-$ and $Uz-$directions equal to fixed and $Ux-$direction equal to free. Likewise, a 47.5 mm of displacement is applied downward in $x-$direction. On the torsional test, the torsional load dimension radius of 0.05 mm and length of 0.5 mm, as seen in Figure 8-c. The fixed support is applied at the end of the torsional test specimen with the translation and rotation constraints applied in the $Ux-$, $Uy-$, and $Uz-$direction and $Rx-$, $Ry-$, and $Rz-$directions equal to fixed, Figure 8-c. Likewise, at the other end of the torsional test specimen, the translation and rotation constraints are applied in the $Ux-$, $Uy-$, and $Uz-$directions, $Ry-$ and $Rz-$directions equal to fixed, and $Rx-$direction equal to free. The simulation ends after the specimen experiences failure. All of the specimens, i.e., for the tensile test, compressive test, and torsional test, are discretized using shell-type elements.

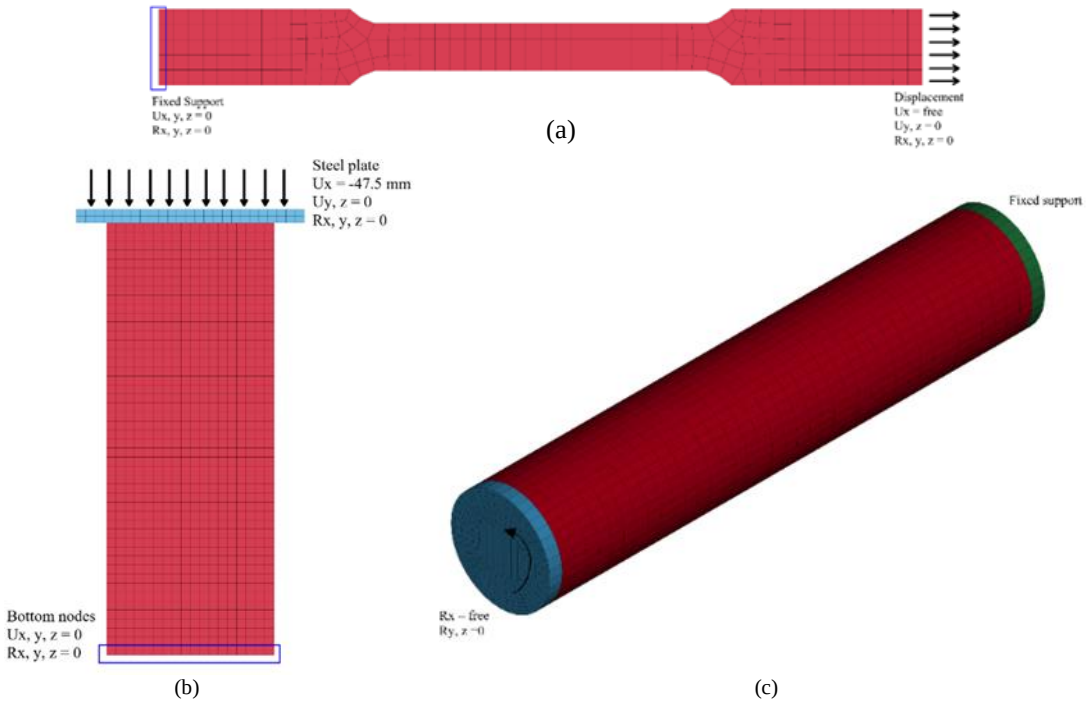

Figure 8. Specimen geometries: (a) tensile test, (b) compressive test, (c) and torsional test

The material properties used for numerical analysis justify the loading scheme presented in Table 1. Aluminum is used for the compressive and torsional tests, and steel SAE 1045 is used for the tensile test. The mechanical properties of aluminum are the following: density ρ = 2700 kg/m^3, Young's modulus E = 68 GPa, and Poisson's ratio ν = 0.33. Moreover, the mechanical properties of steel SAE 1045 are the following: density ρ = 7870 kg/m^3, Young's modulus E = 206 GPa, and Poisson's ratio ν = 0.29. The scheme of finite element analysis is illustrated in Figure 9, which is divided into three stages: pre-processing, processing, and post-processing. For data forecasting, the effect of input parameters (failure criteria and loading scheme) on the output parameter of occurred damage mode will be investigated using nonlinear finite element analysis.

Table 1. Material properties and loading schemes

Materials	ρ (kg/cm^3)	E (GPa)	ν (-)	Loading scheme
Aluminum	2700	68	0.33	Compressive load Torsional load
Steel SAE 1045	7870	206	0.29	Tensile load

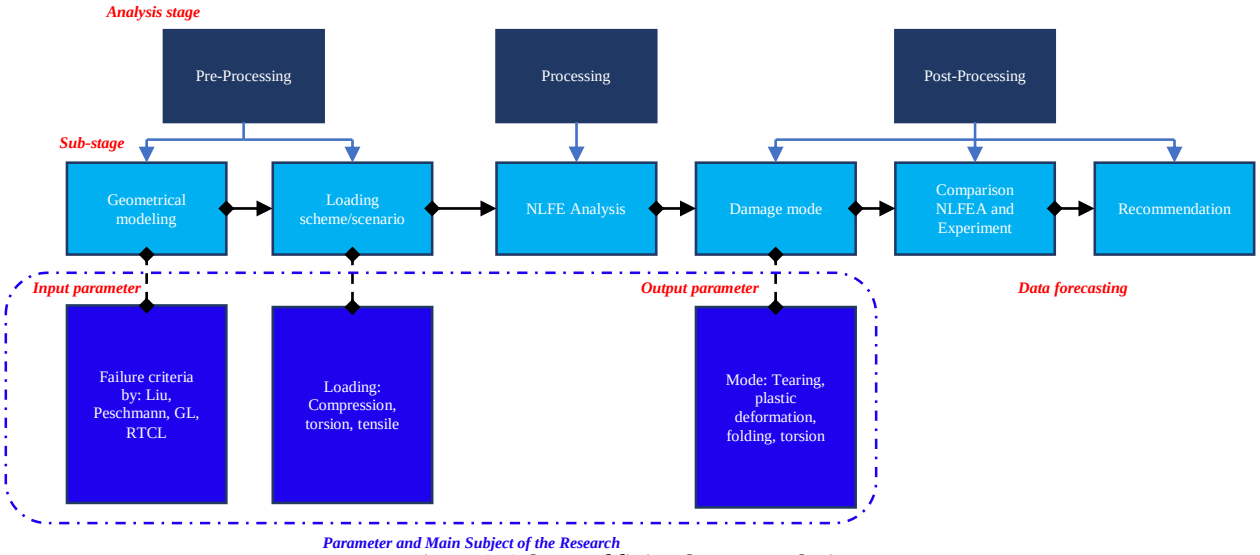

Figure 9. Scheme of finite element analysis

7. Results and Discussion

7.1. Tensile Load

In this section, the numerical results of the tensile test under different failure criteria are presented in Figure 10. The numerical analysis is conducted using 10 different ELT ratios to analyze mesh sensitivity and investigate the validity of the simulation test through comparison with the experimental test. It can be found that varying levels of mesh refinement influence solution convergence. For the analysis of all failure criteria, it is shown that the stress–strain curves obtained from the current simulation and the experimental result are consistent. It can be seen through comparison with the experimental test that larger mesh sizes tend to have higher yield stress. Good agreement of stress–strain curves can be achieved when a smaller ELT ratio is used. Moreover, particular attention is devoted to mesh effects on the crack initiation and rupture strain under different known failure criteria in ship-damaged structures. It also can be seen that all evaluated failure criteria seem to experience a small rupture strain value along with an increase of meshing size. The ELT ratio 8-10 mm (coarser mesh) has the smallest rupture strain.

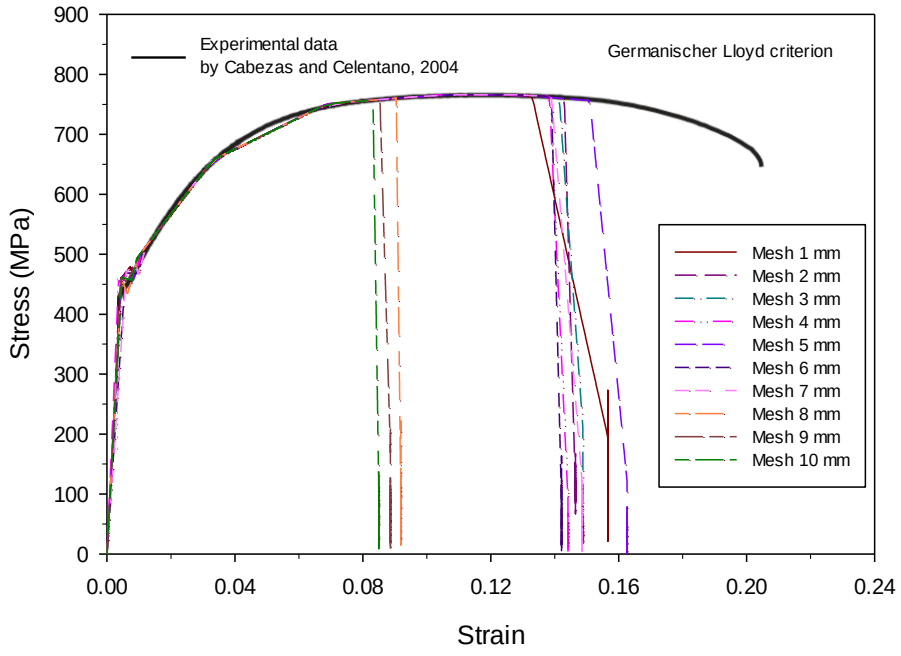

(a) GL

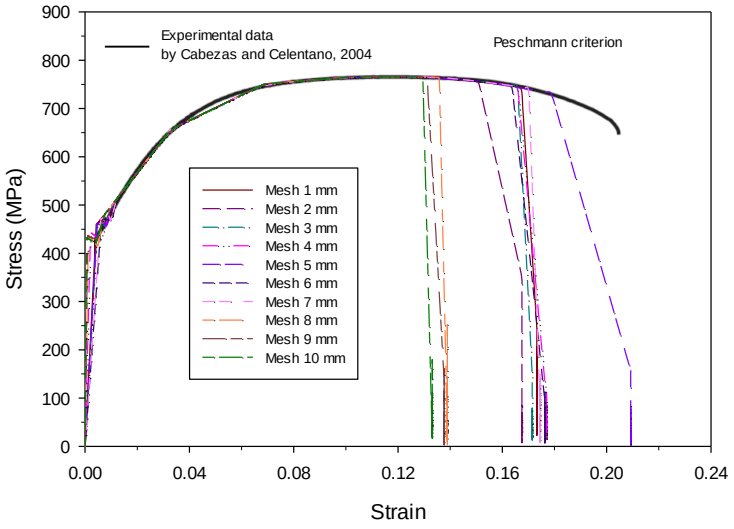

(b) Peschmann

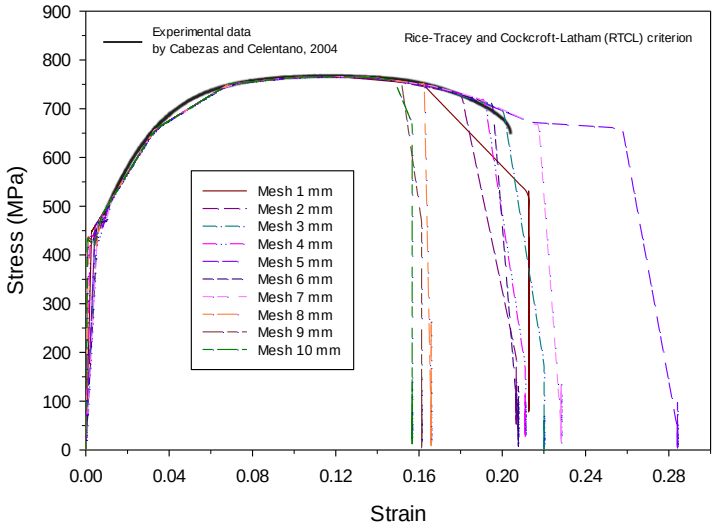

(c) RTCL

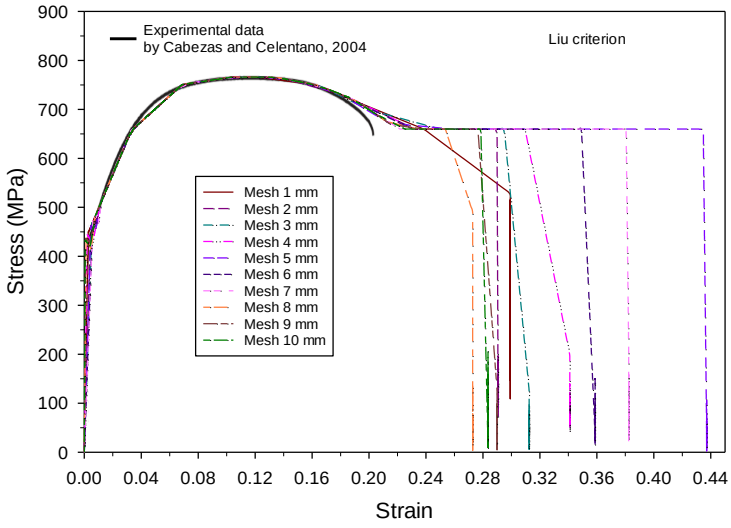

(d) LIU

Figure 10. The tensile stress–strain curve with different mesh sizes under different failure criteria

In the analysis of failure criteria, the LIU failure criterion has considerably highest rupture strain followed by RTCL, Peschmann, and GL criteria. Compared to rupture strain in the experimental test, LIU damage criterion has significantly larger fracture strain for all evaluated ELT ratios. Good agreement cannot be found using these damage criteria. However, for the Peschmann and GL damage criteria, there is a slightly lower rupture strain when comparing with the experimental results. A good agreement can be achieved when using RTCL damage criterion with a fine mesh size (< 7 mm ELT ratio). It is also found that a slightly larger rupture strain is produced when the damage criterion is based on the maximum stress rather than the maximum strain criterion.

In this section, a comparison of the plastic strain distribution after fracture under the same mesh size for the four different failure criteria is depicted in Figure 11. As it is seen, the damage fracture is experienced in the same location, namely in the side of the gauge length near the radius, which means that the damage and the maximum plastic strain are mainly concentrated in this region. This part experiences a concentration of high stress, which is responsible for the necking phenomenon (localized necking) and, finally, the fracture point on the specimen. The comparison of maximum effective strain value shows that LIU has the highest value (0.417), followed by RTCL (0.289), Peschmann (0.190), and GL (0.157).

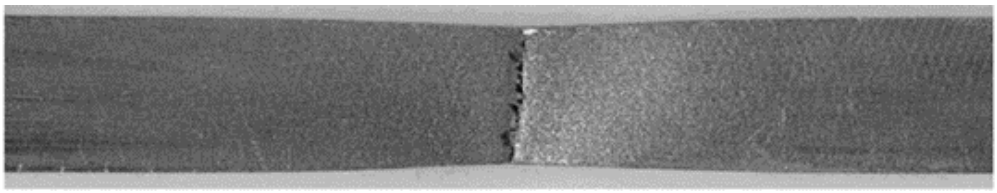

(a) Experimental test [24]

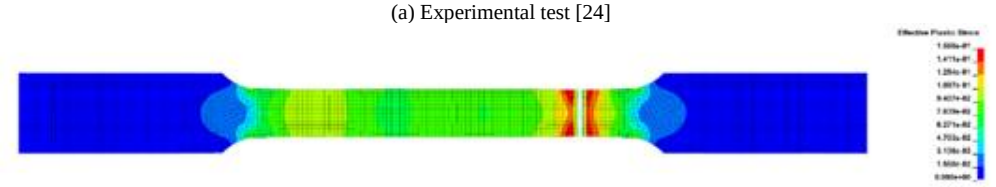

(b) GL

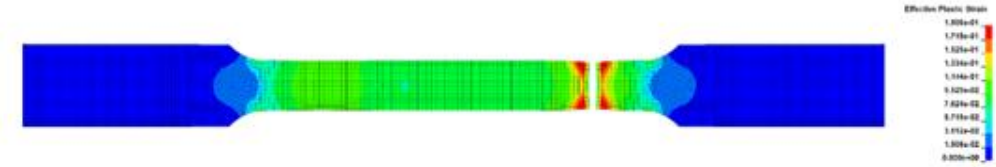

(c) Peschmann

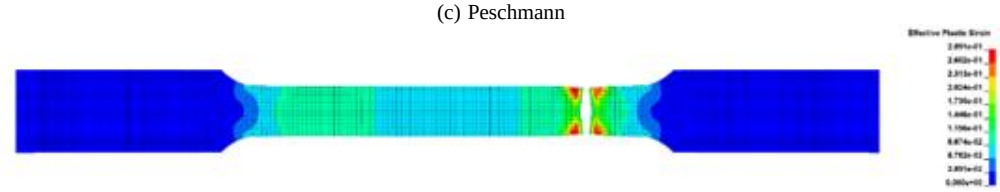

(d) RTCL

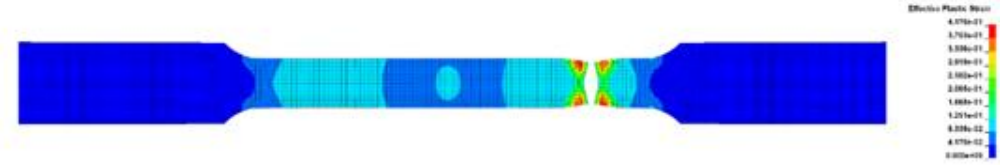

(e) LIU

Figure 11. Plastic strain distribution in the tensile test after fracture occurs under different failure criteria

7.2. Compressive Load

Further, the compressive test results for a hollow structure under variation of damage criteria are presented in Figure 12. Figure 12 shows the load–displacement graphs between the previous experimental test [25] and numerical FE simulation with 2 mm ELT ratio. From the results, it good agreement regarding the maximum force can be found between the numerical and experimental test results. As observed, the maximum force produced by Germanischer Lloyd (GL), Peschmann, Rice–Tracey and Cockcroft–Latham (RTCL), and LIU criteria appears at approximately 29.31, 29.33, 29.35, and 31.22 kN compared to the experimental value of 31.14 kN, respectively, corresponding to percentage differences of 6.05, 5.98, 5.91, and 0.25% in terms of maximum force. The discovered discrepancies are ascribed to numerical inaccuracy as well as imperfections. These imperfections are not taken into account by LS-DYNA. Although an ideal model was created, manufacturing and alignment variations are unavoidable in the actual world, and thus

random geometrical defects are fairly normal in structures. The predicted load–displacement behavior with the experimental observation reveals a good correlation between curves, especially for RTCL damage criterion. In contrast, LIU has the highest load–displacement discrepancies with experimental data.

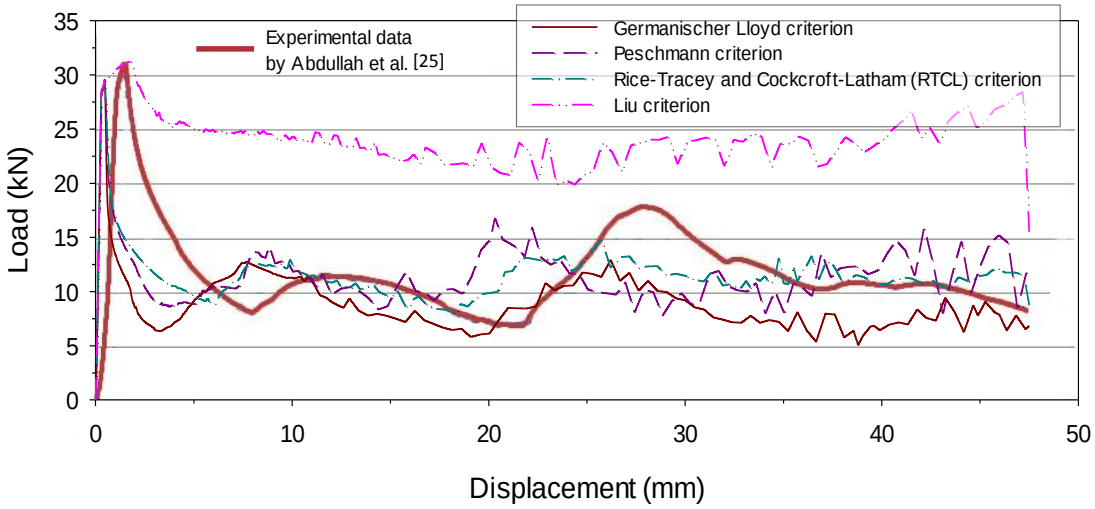

Figure 12. The compressive load–displacement curve under different failure criteria

The finite element analysis and experimental data are compared in terms of deformation mode. Both front and top view are presented side by side. Figure 13 illustrates the progressive collapse of the finite element model with the test specimen at the final stages of compression. As shown in Figure 13, Germanischer Lloyd (GL), Peschmann, Rice–Tracey and Cockcroft–Latham (RTCL), and LIU criterion seem to vary in the production of contour plastic strain. The experimental data and finite element results also show the folding phenomenon occurring after compression. A visual check of the collapse mode reveals good agreement between the results of numerical models and the experimental results. The collapse mode shows specimens deform according to a purely symmetric deformation mode in numerical simulation with RTCL, Peschmann, and GL failure criterion. In contrast, significant discrepancies in the collapse mode compared to the experimental test are found for LIU failure criterion.

(a) Experimental test [25]

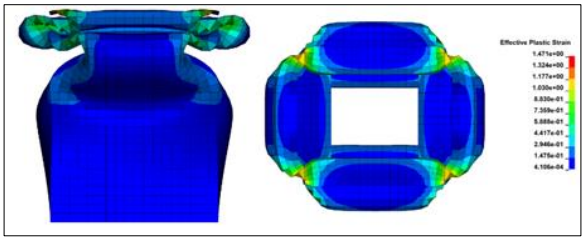

(b) GL

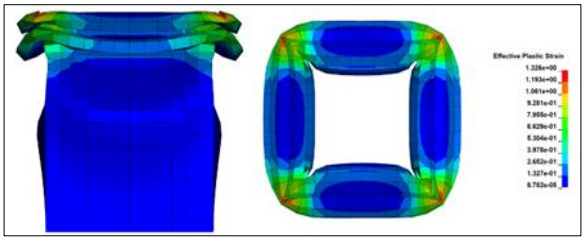

(c) Peschmann

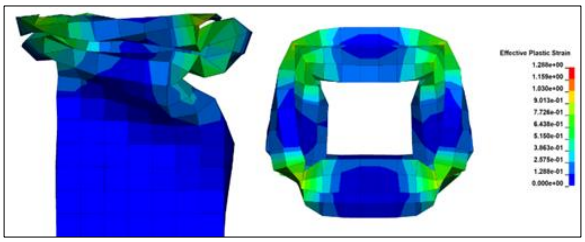

(d) RTCL

(e) LIU

Figure 13. Plastic strain distribution in the compressive test after a fracture occurs under different failure criteria

7.3. Torsional Load

In the last stage, the influence of failure criteria on the damage mode is analyzed by conducting a torsional test subjected to axial torsion on an axisymmetric cylindrical specimen. Numerical FE simulation is performed using four failure criteria with the same mesh size (2 mm ELT ratio). The purpose of a torsion test is to determine the behavior of a material when twisted, especially shear stress–strain behavior and shear strain distribution. Figure 14 shows shear stress–strain graphs under different failure criteria. Most ductile materials exhibit strain hardening wherein the plastic region and the shear stress monotonically increase with a shear strain before fracture. In plastic deformation, it can be found that LIU failure criterion has the largest maximum shear stress and strain. As shown in Figure 14, Germanischer Lloyd (GL), Peschmann, Rice–Tracey and Cockcroft–Latham (RTCL), and LIU criterion produce shear stress at approximately 460.44, 460.09, 459.72, and 534.95 MPa, respectively. These results show that the LIU criterion produces a slightly larger (around 15.12%) maximum shear stress. Moreover, the other failure criteria experience the same plastic behavior.

The result is consistent with two previous tests showing that LIU damage criterion results in the largest discrepancies of all examined criteria. To describe the result more comprehensively, Figure 15 shows the comparison of von Mises stress distribution under twisting load after failure. Failure can be found at the bottom of axisymmetric cylindrical specimens near fixed support. Moreover, a similar result can be found where the highest von Mises stress experiences by Peschmann and GL (409 MPa), followed by RTCL (398 MPa), and LIU damage criterion (273 MPa). The experimental data for torsion load can be seen in Figure 16 and the fracture specimen in Figure 17. As shown in Figure 16, the temperature applied to the torsional test specimen seems to affect the shear stress strength significantly. A low shear stress–strain curve is produced by high temperatures [30].

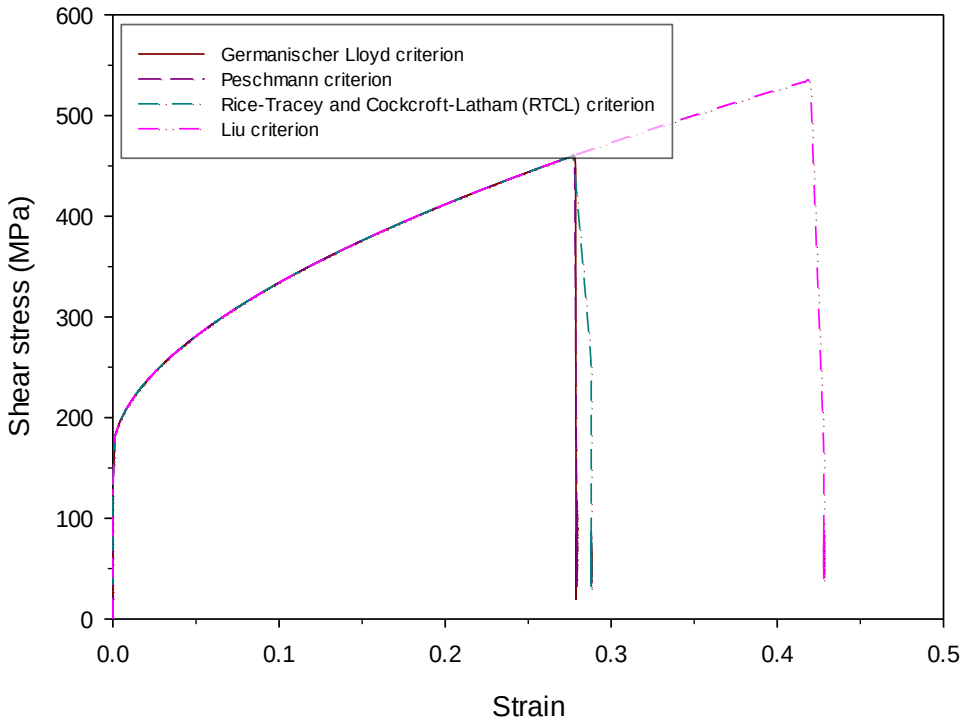

Figure 14. The shear stress–strain curve under different failure criteria

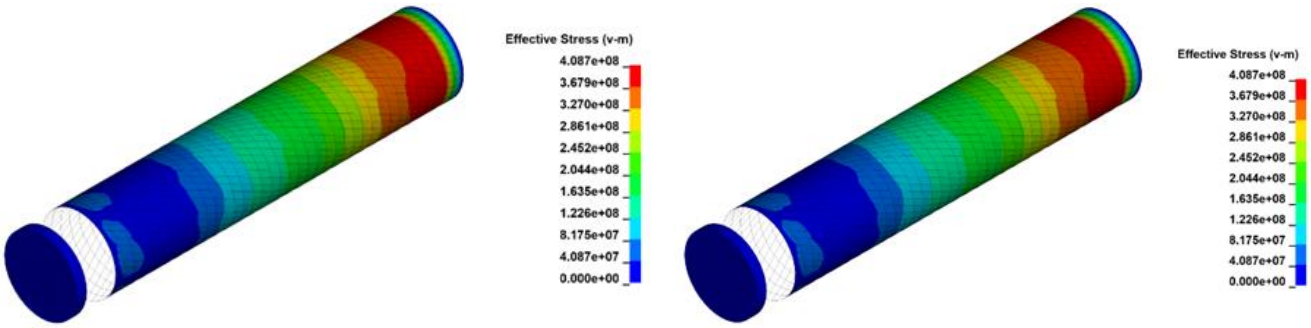

(a) GL (b) Peschmann

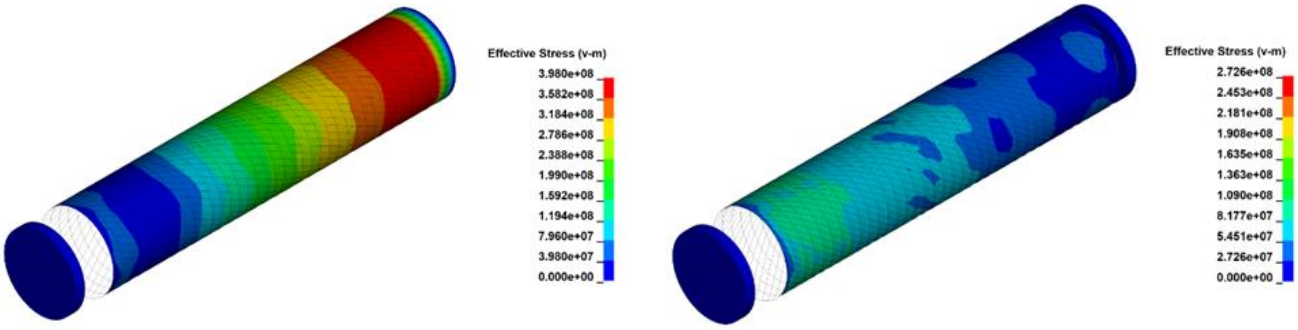

(c) RTCL (d) LIU

Figure 15. Von-mises stress distribution in the torsional test under different failure criteria

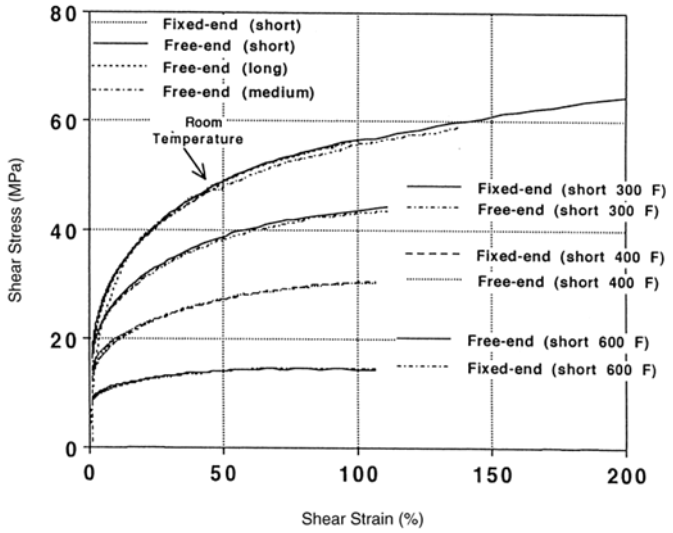

Figure 16. Shear stress–strain curves from the material cast aluminum [30]

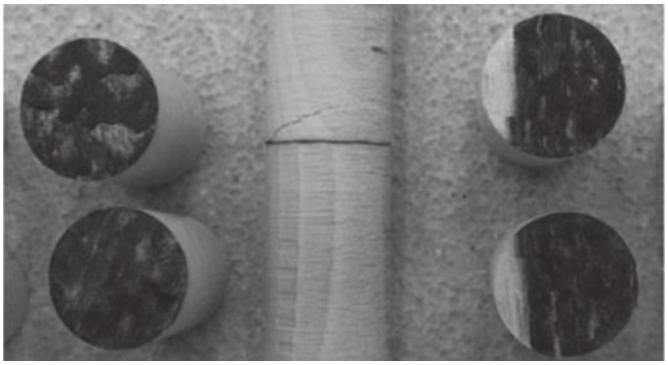

Figure 17. Torsional test experiment data [31]

7.4. Discussion

In this study, we carried out a numerical study of damage, including analysis of tearing, plastic deformation, folding, and torsion with the tensile test, compressive load, and torsional load under different failure criteria, i.e., Germanischer Lloyd (GL), Peschmann, Rice-Tracey, and Cockcroft–Latham (RTCL), and LIU. The numerical results suggest that the selection of failure criteria seems to affect the damage modes, e.g., tearing, plastic deformation, folding, and torsion. A higher value of failure strain (0.417) is determined for the LIU criterion than the Germanischer Lloyd (GL) (0.157), Peschmann (0.190), and Rice–Tracey and Cockcroft–Latham (RTCL) (0.289) criteria. This indicates that larger plastic strain has occurred before tearing failure. Therefore, a moderately immense necking phenomenon appears near the failure area when the LIU criterion is used (Figure 11-e). This study also shows that a slightly larger failure strain is produced with the Peschmann criterion than the Germanischer Lloyd criterion. This result is in accordance with Storheim et al. (2015) [18], which also shows a larger failure strain for the Peschmann criterion than the Germanischer Lloyd criterion. Coarse mesh size appears to transform the failure strain to a small value. In terms of folding damage, this study shows that the failure criteria affect folding damage and load versus displacement. An indication can be observed in the simulation of a compressive load on the hollow tube in Section 7-2. LIU has the highest load versus displacement

discrepancies with experimental data (Figure 12). As observed in Figure 12, the load versus displacement curve has certain peaks that appear during the compressive load. The beginning of pressing shows where the compressive load reaches an initial peak. This indicates that the specimen is carrying its maximum load. After the initial peak, the load falls very sharply and then periodically fluctuates.

The fluctuations in the load are caused by the formation of successive folding events, in which each subsequent peak corresponds to the onset of a folding process. These phenomena on the maximum load and the folding process, which are related to load fluctuation, are also evident in the case of the tube under compressive load as examined by [26, 32, 33]. For torsion damage, Germanischer Lloyd (GL), Peschmann, Rice–Tracey, and Cockcroft–Latham (RTCL) produce shear stress at approximately the same stress: 460.44, 460.09, and 459.72 MPa, respectively. For the LIU criterion, however, this occurs at a slightly higher stress of 534.95 MPa; alternatively, the percentage difference is around 15.12%, Figure 14. The findings for torsion damage mode share similarities with those in the literature [31]. However, slightly more twisting due to the large failure strain is observed in the LIU results. Despite the findings in this study, there are shortcomings in the simulations, which have been carried out such that specimen imperfections are not taken into account by LS-DYNA, in addition to only a few material types being studied and the lack of combined loading schemes. In future work, therefore, the analyses will be conducted using different types of material and combined loading schemes.

8. Conclusion

The numerical evaluation of several failure criteria to investigate the behavior distinction between four different criteria, including Peschmann (P), Germanischer Lloyd (GL), Liu (LIU), and Rice–Tracey and Cockroft–Latham (RTCL), was conducted with variations in the loading scheme. The loading schemes undertaken in this study are compression, torsion, and tensile tests. The results show that there are large discrepancies compared with experimental tests when modeling using the LIU failure criterion. It is also found that a slightly higher rupture strain is produced when the failure criterion is based on maximum stress rather than maximum strain. LIU, Rice–Tracey, Cockcroft–Latham (RTCL), Peschmann, and Germanischer Lloyd (GL) criteria achieved the order of the highest rupture strain discrepancy values. Moreover, the selection of the mesh size was also considered, where the use of a coarser mesh size was shown to result in a smaller rupture strain. Based on this work, recommendations are formulated according to the forecast tendency and accuracy observed for each damage mode exposed to the various failure criteria. In future work, analyses will be conducted using different types of material and combined loading schemes.

9. Declarations

9.1. Author Contributions

Conceptualization, R.R., T.T., F.I., and A.R.P.; methodology, R.R., T.T., and A.R.P.; software, R.R., F.I., and A.R.P.; validation, R.R., T.T., and A.R.P.; formal analysis, R.R. and A.R.P.; investigation, R.R., T.T., F.I., and A.R.P.; resources, F.I., and A.R.P.; data curation, R.R. and T.T.; writing—original draft preparation, R.R., T.T., F.I., and A.R.P.; writing—review and editing, R.R., T.T., and A.R.P.; visualization, R.R. and T.T.; supervision, F.I. and A.R.P.; project administration, F.I. and A.R.P.; funding acquisition, F.I. and A.R.P. All authors have read and agreed to the published version of the manuscript.

9.2. Data Availability Statement

The data presented in this study are available on request from the corresponding author.

9.3. Funding

This work was supported by the RKAT PTNBH Universitas Sebelas Maret Year 2022, under the Research Scheme of “Penelitian Fundamental” (PF-UNS), with research grant/contract no. 254/UN27.22/PT.01.03/2022. The support is gratefully acknowledged by the authors.

9.4. Conflicts of Interest

The authors declare no conflict of interest.

10. References

[1] United Nations Conference on trade and Development (UNCTAD). (2021). Review of Maritime Transport 2021. United Nations Publication, Geneva, Switzerland.

[2] Allianz. (2021). Safety and shipping review 2021. Allianz Global Corporate & Specialty, Munich, Germany.

[3] Ridwan, Putranto, T., Laksono, F. B., & Prabowo, A. R. (2020). Fracture and damage to the material accounting for transportation crash and accident. Procedia Structural Integrity, 27(2020), 38–45. doi:10.1016/j.prostr.2020.07.006.

[4] Prabowo, A. R., Tuswan, T., Prabowoputra, D. M., & Ridwan, R. (2021). Deformation of designed steel plates: An optimization of the side hull structure using the finite element approach. Open Engineering, 11(1), 1034–1047. doi:10.1515/eng-2021-0104.

[5] Fajri, A., Prabowo, A. R., & Muhayat, N. (2022). Assessment of ship structure under fatigue loading: FE benchmarking and extended performance analysis. Curved and Layered Structures, 9(1), 163–186. doi:10.1515/cls-2022-0014.

[6] Prabowo, A. R., Tuswan, T., & Ridwan, R. (2021). Advanced development of sensors' roles in maritime-based industry and research: From field monitoring to high-risk phenomenon measurement. Applied Sciences (Switzerland), 11(9), 3954. doi:10.3390/app11093954.

[7] Ansori, D. T. A., Prabowo, A. R., Muttaqie, T., Muhayat, N., Laksono, F. B., Tjahjana, D. D. D. P., Prasetyo, A., & Kuswardi, Y. (2022). Investigation of Honeycomb Sandwich Panel Structure using Aluminum Alloy (AL6XN) Material under Blast Loading. Civil Engineering Journal (Iran), 8(5), 1046–1068. doi:10.28991/CEJ-2022-08-05-014.

[8] Minorsly, V. U. (1959). An Analysis of ship Collisions with Reference to Protection of Nuclear Power Plants.pdf. Journal of Ship Research, 3(2), 1–4.

[9] Lehmann, E., & Peschmann, J. (2002). Energy absorption by the steel structure of ships in the event of collisions. Marine Structures, 15(4–5), 429–441. doi:10.1016/S0951-8339(02)00011-4.

[10] Scharrer, M., Zhang, L., & Egge, E.-D. (2002). Abschlußbericht zum Vorhaben MTK0614, Kollisionsberechnungen in schiffbaulichen Entwurfssystemen (Collision calculations in naval engineering design systems). Version 1/2002-11-22. Bericht Nr. ESS 202.183; Version 1/2002-11-22, Hamburg, Germany.

[11] Törnqvist, R. (2003). Design of crashworthy ship structures. PhD Thesis, Department of Mechanical Engineering, Technical University of Denmark, Lyngby, Denmark.

[12] Liu, B., Villavicencio, R., Zhang, S., & Guedes Soares, C. (2017). A simple criterion to evaluate the rupture of materials in ship collision simulations. Marine Structures, 54, 92–111. doi:10.1016/j.marstruc.2017.03.006.

[13] Alwan, F. H. A., Prabowo, A. R., Muttaqie, T., Muhayat, N., Ridwan, R., & Laksono, F. B. (2022). Assessment of ballistic impact damage on aluminum and magnesium alloys against high velocity bullets by dynamic FE simulations. Journal of the Mechanical Behavior of Materials, 31(1), 595–616. doi:10.1515/jmbm-2022-0064.

[14] Ehlers, S., Broekhuijsen, J., Alsos, H. S., Biehl, F., & Tabri, K. (2008). Simulating the collision response of ship side structures: A failure criteria benchmark study. International Shipbuilding Progress, 55(1–2), 127–144. doi:10.3233/ISP-2008-0042.

[15] Alsos, H. S., Amdahl, J., & Hopperstad, O. S. (2009). On the resistance to penetration of stiffened plates, Part II: Numerical analysis. International Journal of Impact Engineering, 36(7), 875–887. doi:10.1016/j.ijimpeng.2008.11.004.

[16] Marinatos, J. N., & Samuelides, M. S. (2015). Towards a unified methodology for the simulation of rupture in collision and grounding of ships. Marine Structures, 42, 1–32. doi:10.1016/j.marstruc.2015.02.006.

[17] Abubakar, A., & Dow, R. S. (2013). Simulation of ship grounding damage using the finite element method. International Journal of Solids and Structures, 50(5), 623–636. doi:10.1016/j.ijsolstr.2012.10.016.

[18] Storheim, M., Amdahl, J., & Martens, I. (2015). On the accuracy of fracture estimation in collision analysis of ship and offshore structures. Marine Structures, 44, 254–287. doi:10.1016/j.marstruc.2015.09.006.

[19] Sèbe, M., Kontovas, C. A., & Pendleton, L. (2020). Reducing whale-ship collisions by better estimating damages to ships. Science of the Total Environment, 713, 136643. doi:10.1016/j.scitotenv.2020.136643.

[20] Callister Jr, W. D. (2000). Materials Science and Engineering-An Introduction (5th Ed.). John Wiley & Sons, Hoboken, United States. doi:10.1108/acmm.2000.12847aae.001.

[21] ANSYS. (2020). ANSYS LS-DYNA User's Guide. ANSYS, Inc., Pennsylvania, United States.

[22] Rice, J. R., & Tracey, D. M. (1969). On the ductile enlargement of voids in triaxial stress fields. Journal of the Mechanics and Physics of Solids, 17(3), 201–217. doi:10.1016/0022-5096(69)90033-7.

[23] Cockcroft, M. G., & Latham, D. J. (1968). Ductility and the workability of metals. Journal of the Institute of Metals, 96(1), 33–39.

[24] Cabezas, E. E., & Celentano, D. J. (2004). Experimental and numerical analysis of the tensile test using sheet specimens. Finite Elements in Analysis and Design, 40(5–6), 555–575. doi:10.1016/S0168-874X(03)00096-9.

[25] Abdullah, K. A., Mohamed Ali, J. S., & Aminanda, Y. (2012). Experimental and numerical simulation of hollow structure under compression loading. Advanced Materials Research, 576, 651–654. doi:10.4028/www.scientific.net/AMR.576.651.

[26] Ridwan, R., Nuriana, W., & Prabowo, A. R. (2022). Energy absorption behaviors of designed metallic square tubes under axial loading: Experiment-based benchmarking and finite element calculation. Journal of the Mechanical Behavior of Materials, 31(1), 443–461. doi:10.1515/jmbm-2022-0052.

[27] Prabowo, A. R., Ridwan, R., & Muttaqie, T. (2022). On The Resistance to Buckling Loads of Idealized Hull Structures: FE Analysis on Designed-Stiffened Plates. Designs, 6(3), 46. doi:10.3390/designs6030046.

[28] Widiyanto, I., Alwan, F. H. A., Mubarok, M. A. H., Prabowo, A. R., Laksono, F. B., Bahatmaka, A., Adiputra, R., & Smaradhana, D. F. (2021). Effect of geometrical variations on the structural performance of shipping container panels: A parametric study towards a new alternative design. Curved and Layered Structures, 8(1), 271–306. doi:10.1515/cls-2021-0024.

[29] Dzulfiqar, M. F., Prabowo, A. R., Ridwan, R., & Nubli, H. (2021). Assessment on the designed structural frame of the automatic thickness checking machine - Numerical validation in FE method. Procedia Structural Integrity, 33(C), 59–66. doi:10.1016/j.prostr.2021.10.009.

[30] Wu, H. C., Xu, Z., & Wang, P. T. (1997). Torsion test of aluminum in the large strain range. International Journal of Plasticity, 13(10), 873–892. doi:10.1016/S0749-6419(97)00064-8.

[31] Rhême, M., Botsis, J., Cugnoni, J., & Navi, P. (2013). Influence of the moisture content on the fracture characteristics of welded wood joint. Part 2: Mode II fracture. Holzforschung, 67(7), 755–761. doi:10.1515/hf-2012-0145.

[32] Salehghaffari, S., Tajdari, M., Panahi, M., & Mokhtarnezhad, F. (2010). Attempts to improve energy absorption characteristics of circular metal tubes subjected to axial loading. Thin-Walled Structures, 48(6), 379–390. doi:10.1016/j.tws.2010.01.012.

[33] Lu, G., & Yu, T. (2003). Energy Absorption of Structures and Materials. Woodhead Publishing Limited, Cambridge, England. doi:10.1533/9781855738584.